

# Analysis of parameter effects on chemical reaction coupled transport phenomena in SOFC anodes

Jinliang Yuan · Yuan Huang · Bengt Sundén ·  
Wei Guo Wang

Received: 7 March 2008 / Accepted: 18 September 2008 / Published online: 15 October 2008  
© Springer-Verlag 2008

**Abstract** Mass, heat and momentum transport processes are strongly coupled by internal chemical reforming reactions in planar design solid oxide fuel cell (SOFC) anodes. In this paper, a three-dimensional computational fluid dynamics approach is applied to simulate and analyze reforming reactions of methane and various transport processes in a duct relevant for SOFC anodes. The results show that the anode duct design and operating parameters, grouped as three characteristic ratios, are significant for the chemical reactions and further for multi-species distribution, fuel gas transport and heat transfer in the sub-domains of the anode.

## List of symbols

$A_{\text{active}}$	surface area of control volume at active site ( $\text{m}^2$ )
$a$	width of porous layer (m)
$B$	inertial coefficient
$b$	width of flow duct (m)
$c_p$	specific heat capacity ( $\text{J/kg K}$ )
$D$	molar diffusion coefficient of fuel gas species ( $\text{m}^2/\text{s}$ )
$E_a$	activation energy ( $\text{kJ/mol}$ )
$H$	enthalpy ( $\text{kJ/mol}$ )

$h$	overall height of the duct (m)
$h_d$	height of the duct (m)
$h_p$	thickness of porous layer (m)
$J$	electrochemical reaction related molar flux ( $\text{mol/m}^2 \text{ s}$ )
$K_e$	equilibrium constants ( $\text{Pa}^2$ )
$k$	thermal conductivity, $\text{W}/(\text{m K})$ ; reaction rate constant ( $\text{mol/m}^3 \text{ Pa}^2 \text{ s}$ )
$k_0$	pre-exponential constant
$M$	molecular weight of species ( $\text{kg/mol}$ )
$\dot{m}$	mass diffusion flux ( $\text{kg/m}^2 \text{ s}$ )
$\dot{n}$	molar diffusion flux ( $\text{mol/m}^2 \text{ s}$ )
$n$	total number of species
$P$	pressure (Pa)
$q$	heat flux ( $\text{W/m}^2$ )
$R$	internal reforming reaction rate ( $\text{mol/m}^3 \text{ s}$ )
$\mathfrak{R}$	gas constant, ( $\text{kJ/mol K}$ )
$Re$	Reynolds number ( $UD_h/\nu$ )
$r_e$	effective radius (m)
$S$	source term
$T$	temperature, $^\circ\text{C}$
$\mathbf{v}$	velocity vector (m/s)
$V_i$	velocity components in $x$ , $y$ and $z$ directions, respectively (m/s)
$X$	molar fraction of fuel species
$Y$	mass fraction of fuel species
$x, y, z$	Cartesian coordinates

J. Yuan (✉) · B. Sundén  
Department of Energy Sciences, Lund University, Box 118,  
22100 Lund, Sweden  
e-mail: Jinliang.yuan@energy.lth.se

Y. Huang · W. G. Wang  
Ningbo Institute of Materials Technology and Engineering  
(NIMTE), Chinese Academy of Sciences (CAS), 315040  
Ningbo, People's Republic of China

## Greek symbols

$\beta$	permeability of porous layer ( $\text{m}^2$ )
$\varepsilon$	porosity
$\mu$	dynamic viscosity ( $\text{kg/m s}$ )
$\nu$	kinematic viscosity ( $\text{m}^2/\text{s}$ )
$\rho$	density ( $\text{kg/m}^3$ )
$\tau$	tortuosity

**Superscripts**

- + forward reaction
- reverse reaction

**Subscripts**

- di diffusion layer
- eff effective parameter
- f* fuel gas mixture
- CH<sub>4</sub> methane
- CO carbon monoxide
- CO<sub>2</sub> carbon dioxide
- e* equilibrium
- gm fuel gas mixture
- H<sub>2</sub> hydrogen
- H<sub>2</sub>O water
- in inlet
- k* Knudsen diffusion
- m* mass transfer
- p* permeation
- r* steam reforming reaction
- s* solid wall; shift reaction; species

**1 Introduction**

High temperature solid oxide fuel cells (SOFCs), with the advantages of high efficiencies, environmental friendliness and flexibility of usable fuel types, have been considered as one of the most promising technologies for electricity energy generation. Many variations of SOFC designs are possible, such as tubular, planar and monolithic. The planar SOFCs have several advantages, such as higher power density, compactness, and simple to be fabricated and manufactured into various configurations [1]. It is a fact that the requirement of high temperature gas seals, internal stresses in cell components is very critical for SOFCs development [1]. One of the new trends is to reduce the operating temperature of solid oxide fuel cells (SOFCs) to an intermediate range (from 1,000 to 800°C) by employing a thick porous layer (1.5–2 mm) as the supporting structure [2–5]. The transport rate of fuel gases in the porous anode is controlled by various parameters, such as porous microstructure (i.e., pore size, permeability, volume percent porosity of the employed porous layer), pressure gradient between the fuel flow duct and the porous anode, gas composition and inlet conditions, etc. [6, 7].

For the case of pure hydrogen being employed as a fuel, part of H<sub>2</sub> is consumed while water vapor (H<sub>2</sub>O) is generated during the electrochemical reaction. If methane is used as the fuel, internal reforming reactions within SOFC anodes enable the conversion of the methane into H<sub>2</sub> and CO. It is a fact that the heat required to keep internal steam reforming can be provided by the electrochemical reactions

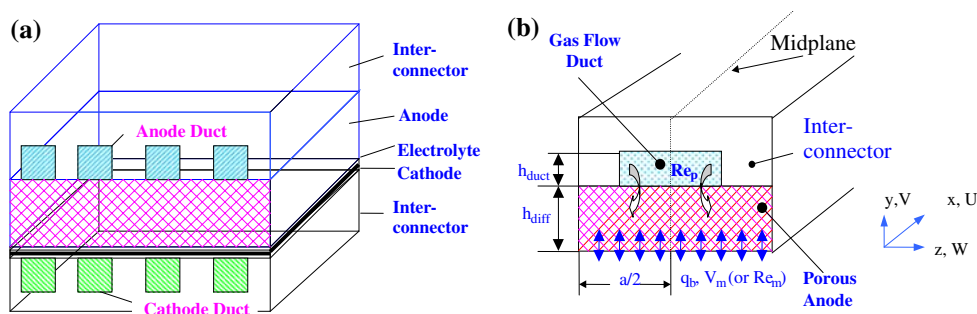
in SOFCs. Several benefits are expected to have internal steam reforming of employed hydrocarbon fuels, for instances, the energy conversion efficiency will be much higher. Moreover, close coupling of the internal reforming and the electrochemical reactions at the anode gives good heat transfer. Furthermore, H<sub>2</sub> and CO are utilized by the cells as soon as they are produced by the reforming reaction, and the steam produced by the electrochemical reaction can be used in the reforming reaction as well [9, 10]. However, most of the internal reforming reactions take place in the porous anode next to the fuel gas flow duct due to the high methane conversion rate, and very little methane reaches the active surface between the electrolyte and the porous anode. The endothermic internal steam reforming reaction and the exothermic electrochemical reactions are separated, and consequently may lead to big temperature gradients in the porous layer.

To deeply understand the effects of design and operating parameters on the chemical-reacting transport processes in the porous anode, a fully three-dimensional numerical calculation procedure (CFD approach) is further developed. The study includes the shift reactions of CO in the porous anodes. The considered duct includes the porous anode, fuel gas flow duct and the solid interconnects. By calculating fuel gas species, the species mass/heat generation and consumption related to the internal reforming reactions and the electrochemical reaction have been identified and employed in the study. The variable thermal-physical properties and transport parameters of the fuel gas mixture have also been taken into account. Furthermore, the heat transfer due to the fuel gas diffusion is implemented into the energy balance based on multi-component diffusion models. One of the objectives of this study is to develop such an approach to understand parameter effects on various transport processes coupled with chemical reactions in the anode ducts of ITSOFCs.

**2 Problem statement and formulations****2.1 Chemical reactions and internal reforming reaction kinetics**

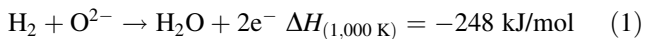
Structure of a unit cell and a schematic drawing of the anode duct are shown in Fig. 1a and b. The *U*, *V*, and *W* are the velocity components in the *x*, *y*, *z* directions, respectively. In this study, the porous anode layer is assumed to be homogeneous and characterized by effective parameters and the fuel species in the porous anode are in thermal equilibrium with the solid matrix. The electrochemical reaction appears at the interface between the electrolyte and the porous layer, i.e., the bottom surface in Fig. 1b, while the internal reforming reactions appear in the porous

**Fig. 1** **a** Structure of a unit cell; **b** schematic drawing of a composite anode duct in ITSOFCs



layer. A constant flow rate  $U = U_{in}$  with a mass fraction of the mixed fuel gas is specified at the inlet of the fuel gas flow duct, while  $U = 0$  is specified at the inlet for inter-connector and the porous anode layer. Only the right half of the duct is considered by imposing symmetry conditions on the mid-plane.

The electrochemical reactions to generate electricity are the oxidation of  $H_2$ :



As revealed in [8], the electrochemical oxidation rate of  $H_2$  is twice or several times higher than that of  $CO$ , while the water–gas shift reaction below is fast enough, and the shift reaction may be in the equilibrium state in the anode. The contribution of  $CO$  oxidation to the cell performance (the total current density) and effects on the transport processes are not considered yet in this study, but will be analyzed when the unit cell including the triple phase layer (TPB) is studied. The above reactions produce a significant amount of water and heat at the anode/electrolyte interface during operation. Methane and carbon monoxide can be internally reformed into  $H_2$  by the following reactions:



Equation 2 is internal steam reforming reaction, while Eq. 3 is usually referred to as water–gas shift reaction. It should be mentioned that the steam reforming reaction is endothermic and the overall balance of the reaction requires net heat input by the electrochemical reactions. As for the kinetics of the methane reforming reaction on nickel cermet SOFC anodes, extensive reviews can be found in [9–11]. It is common to employ the forward kinetic reforming reactions in the following form [9]:

$$k^+ = k_0 F(p_i) \exp\left(-\frac{E_a}{\Re T}\right) \quad (4)$$

where  $\Re$  is the universal gas constant with unit  $J/(\text{mol K})$ ,  $F$  the function of the species partial pressure, while  $E_a$  stands for the activation energy,  $k_0$  the pre-exponential constant. It is revealed that the first order kinetic expression

is considered typical of direct internal reforming reactions in SOFC performance [9, 10]. The following expressions employed in [11] are adopted in this study:

$$k_r^+ = 2395 \exp(-231266/\Re T) \quad (5)$$

$$k_s^+ = 0.0171 \exp(-103191/\Re T) \quad (6)$$

The backward kinetics  $k_r^-$  and  $k_s^-$  can be determined based on the following equilibrium constants  $K_e$  for the two reactions,

$$K_{er} = \frac{k_r^+}{k_r^-}; \quad K_{es} = \frac{k_s^+}{k_s^-} \quad (7)$$

which are functions of temperature given by the following empirical equations [11]:

$$K_{er} = 1.0267 \times 10^{10} \times \exp(-0.2513Z^4 + 0.3665Z^3 + 0.5810Z^2 - 27.134Z + 3.27770) \quad (8)$$

$$K_{es} = \exp(-0.2935Z^3 + 0.6351Z^2 + 4.1788Z + 0.3169) \quad (9)$$

$$Z = \frac{1,000}{T} - 1 \quad (10)$$

### 2.2 Governing equations and source terms

The governing equations to be solved are the continuity, momentum, energy and species equations, as listed in Table 1.

The inclusion of the source term  $S_{di}$  allows the moment equation to be valid for both the porous layer and the fuel gas flow duct, i.e., the source term is zero in the fuel gas flow duct, because the permeability  $\beta$  is infinite. The moment equation then reduces to the regular Navier-Stokes equation. For the porous anode, the source term  $S_{di}$  is not zero, and the momentum equation with the non-zero source term can be regarded as a generalized Darcy model [10].

The species conservation equations are formulated in a general form, in where  $Y_i$  is the mass fraction of the  $i$ th fuel gas species,  $\dot{m}_i$  represents the mass diffusive flux of species in units of  $\text{kg}/(\text{m}^2 \text{ s})$ , and  $S_{s,i}$  the production/consumption rate of the  $i$ th fuel species. This equation is solved for  $H_2$ ,

**Table 1** Governing equations and relevant sources terms

	Governing equations	Sources terms	Subdomain
Continuity equation	$\nabla \cdot (\rho_{\text{eff}} \mathbf{V}) = S_m$	$S_m = (J_{\text{H}_2} + J_{\text{H}_2\text{O}}) \frac{A_{\text{active}}}{V}$ $= \left( -\frac{i_{\text{H}_2}}{2F} M_{\text{H}_2} + \frac{i_{\text{H}_2}}{2F} M_{\text{H}_2\text{O}} \right) \frac{A_{\text{active}}}{V}$	The bottom surface in Fig. 1b
Momentum equation	$\nabla \cdot (\rho_{\text{eff}} \mathbf{V}\mathbf{V}) = -\nabla P + \nabla \cdot (\mu_{\text{eff}} \nabla \mathbf{V}) + S_{\text{di}}$	$S_{\text{di}} = -(\mu_{\text{eff}} \mathbf{v} / \beta)$	Porous anode
Species equation	$\nabla \cdot (\rho_{\text{eff}} \mathbf{V}Y_i) = \nabla \cdot \dot{\mathbf{m}}_i + S_{S,i}$	$S_{S,\text{H}_2} = (3R_r + R_s)M_{\text{H}_2};$ $S_{S,\text{CH}_4} = -R_r M_{\text{CH}_4};$ $S_{S,\text{H}_2\text{O}} = (-R_r - R_s)M_{\text{H}_2\text{O}};$ $S_{S,\text{CO}} = (R_r - R_s)M_{\text{CO}}$	Porous anode
Energy equation	$\rho_{\text{eff}} c_{p,\text{eff}} \nabla \cdot (\mathbf{V}T) = \nabla \cdot \left( k_{\text{eff}} \nabla T - \sum_{i=1}^n \dot{\mathbf{m}}_i h_i \right) + S_T$	$S_T = \sum_i R_i \Delta h_{\text{reaction},i}$	Porous anode

CH<sub>4</sub>, CO and H<sub>2</sub>O, respectively, i.e., for  $n - 1$  species where  $n$  is the total number of species involved in the fuel gas mixture. The last species (CO<sub>2</sub>) can be solved because the sum of the mass fractions equals one.

It is clear that mass diffusion is a process leading to equalization of substance concentration or establishing an equilibrium gas distribution that results from random migration of the species. Molecular diffusion occurs as a result of thermal motion of the molecules, and proceeds at a maximum rate in gases, a lower rate in liquids, and at a still lower rate in solids [12]. In the general case, the molecular diffusion flux of the species  $i$  is proportional to the concentration gradient and diffusion coefficient. One of the significant challenges in SOFC modelling is in determining the rate at which the species diffuse and gases convect in the gas flow ducts and porous electrodes. This requires knowledge of multi-component diffusion in the fuel gas flow ducts, particularly in the porous layers. In the literature, the Stefan-Maxwell model is more commonly used in multi-component system, as in this study. The diffusion coefficients of species  $i$  in the fuel gas flow duct is calculated by the expression based on the binary coefficients [12]

$$D_{A,\text{gm}} = \frac{1 - X_A}{X_B/D_{AB} + X_C/D_{AC} + \dots} \tag{11}$$

where  $D_A$  is the diffusion coefficient of the component  $A$  in the mixture with  $B, C, \dots$ ,  $X_A, X_B, X_C$  are the molar fraction of the appropriate species, and  $D_{AB}$  and  $D_{AC}$  are the diffusion coefficients in the  $AB$  and  $AC$  binary system, respectively. It is clear that for an  $n$  component system,  $n(n - 1)/2$  binary diffusivities are required.

For the porous layer, molecular diffusion is predominant in the case with large pores, whose size is much bigger than the free-path of the diffusion gas molecules. In this case, the diffusion can be described as above presented for the fuel gas flow duct. Knudsen diffusion occurs in the porous layer with small pores or under low pressure when the mean free-path of molecules is smaller than the pore size,

and the molecules collide with the walls more often than between themselves. In order to calculate the Knudsen diffusion flux, the coefficient  $D_{i,k}$  is calculated based on the free molecule flow theory [12]:

$$D_{i,k} = \frac{2}{3} r_e v_i = \frac{2}{3} r_e \sqrt{\frac{8RT}{\pi M_i}} \tag{12}$$

in which  $r_e$  is the effective radius and  $v_i$  the average molecular speed of the  $i$ th fuel species. To account for the reduction in the cross-sectional area and the increased diffusion length due to the tortuous paths of real pores in the porous anode, the effective diffusion coefficient can be evaluated [11, 12]:

$$D_{i,\text{eff}} = \frac{\varepsilon}{\tau} \left( \frac{D_{i,\text{gm}} \times D_{i,k}}{D_{i,\text{gm}} + D_{i,k}} \right) \tag{13}$$

where  $\varepsilon$  is the porous anode porosity,  $\tau$  tortuosity.

The most common anode is based on nickel/zirconia cermet which can provide sufficient activity for the steam reforming and the water–gas shift reactions [11]. There exist various reaction kinetics and rate/equilibrium constants reported in the literature for both the steam reforming and water–gas shift reactions. However, based on extensive reviews in [10, 11, 13], it can be found that the rate data presented in the literature varies greatly due to the use of different material structures and different amount of catalyst. In this study, the following reaction rates are employed to express the kinetic rates of absorption or production of the fuel gas species, based on partial pressure, temperature and species compositions:

$$R_r = k_r^+ p_{\text{CH}_4} p_{\text{H}_2\text{O}} - k_r^- p_{\text{CO}} (p_{\text{H}_2})^3 \tag{14}$$

$$R_s = k_s^+ p_{\text{CO}} p_{\text{H}_2\text{O}} - k_s^- p_{\text{CO}_2} p_{\text{H}_2} \tag{15}$$

in which,  $k^+$  and  $k^-$  are velocity constants of the forward and backward reactions,  $p$  partial pressure. The energy equation balances the convected energy, the heat conduction through the solid and the fuel gas mixture (heat conduction), the energy due to fuel gas species

diffusion, and a source term  $S_T$ . In which  $h_i$  is the partial enthalpy of the  $i$ th species and is obtained from [11]:

$$h_i = h_{\text{form},i} + \int_{T_0}^T c_{p,i}(T) dT \quad (16)$$

where  $h_{\text{form},i}$  is the specific enthalpy of formation of the  $i$ th fuel species at  $T = T_0 = 298.15$  K. The heat source term  $S_T$  in the energy equation is associated with the steam reforming and water–gas shift reactions. It should be noted that all thermal-physical and transport parameters with subscript eff are the effective ones, and reduce to the values of the fuel gas mixture in the fuel gas flow duct based on the fuel species composition. However, for the porous anode the effective density is simply evaluated by  $\rho_f$  of the fuel gas mixture ( $\text{H}_2 + \text{CH}_4 + \text{CO} + \text{H}_2\text{O} + \text{CO}_2$ ), while, the effective transport parameters, such as thermal conductivity  $k_{\text{eff}}$  and specific heat  $c_{p,\text{eff}}$ , are estimated by considering the porous layer effects:

$$k_{\text{eff}} = \varepsilon k_f + (1 - \varepsilon) k_s \quad (17)$$

$$c_{p,\text{eff}} = \varepsilon c_{p,f} + (1 - \varepsilon) c_{p,s} \quad (18)$$

### 2.3 Boundary and interface conditions

Based on the ITSOFC function, the thermal and fuel gas mass concentration/flux boundary conditions at the walls are specified as follows, i.e.,

at the bottom wall ( $y = 0$ ):

$$\begin{aligned} U = V - V_m = W = 0; \quad q_b = -k_{\text{eff}} \frac{\partial T}{\partial y}; \\ J_i = -\rho_{\text{eff}} D_{i,\text{eff}} \frac{\partial Y_i}{\partial y} \quad (i = \text{H}_2 \text{ and } \text{H}_2\text{O}) \text{ and} \\ J_i = 0 \quad (i = \text{CO} \text{ and } \text{CH}_4) \end{aligned} \quad (19)$$

at the top and side walls:

$$U = V = W = 0, \quad q = 0, \quad J_i = 0 \quad (20)$$

at the mid-plane ( $z = a/2$ ):

$$\frac{\partial U}{\partial z} = \frac{\partial V}{\partial z} = W = \frac{\partial T}{\partial z} = \frac{\partial Y_i}{\partial z} = 0 \quad (21)$$

In the present investigation, the interfacial boundary conditions, commonly employed in the literature, are applied for the continuity of shear stress, heat flux and mass flux:

$$(\mu_{\text{eff}} \partial U / \partial y)_- = (\mu_f \partial U / \partial y)_+ \quad (22)$$

$$(k_{\text{eff}} \partial T / \partial y)_- = (k_f \partial T / \partial y)_+ \quad (23)$$

$$(\rho_{\text{eff}} D_{i,\text{eff}} \partial Y_i / \partial y)_- = (\rho_f D_{i,\text{gm}} \partial Y_i / \partial y)_+ \quad (24)$$

Here subscript + (plus) stands for fluid side, – (minus) for the porous layer side. Moreover, the thermal interfacial

condition, Eq. 23, is also applied at an interface between the porous anode and the solid current interconnect with  $k_s$  instead of  $k_f$ .

### 3 CFD approach and solutions

A three-dimensional CFD code is further developed and employed to solve the governing equations in Table 1, together with the boundary conditions (Eqs. 19–21) and interfacial conditions (Eqs. 22–24). The code is a general purpose one based on the finite-volume technique with boundary fitted coordinates for solving the differential equations. The momentum equations are solved for the velocity components on a non-staggered grid arrangement. The Rhie-Chow interpolation method is used to compute the velocity components at the control volume faces. Algorithms based on the TDMA (Tri-Diagonal Matrix Algorithm) and a modified SIP (strongly implicit procedure) are employed for solving the algebraic equations. The convective terms are treated by the quadratic upstream interpolation convective kinematics (QUICK) scheme, while the diffusive terms are treated by the central difference scheme. The semi-implicit method for pressure-linked equations-consistent (SIMPLEC) algorithm handles the linkage between velocities and pressure.

As shown above, the equations needed for the calculation are coupled by the current density, temperature, fuel species partial pressure/concentration via source terms and variable physical/transport properties. It should be noted that the source term in the continuity equation is zero in most of the regions, and non-zero only in the regions neighboring boundaries, where mass transfer caused by the electrochemical reaction occurs (the bottom wall in Fig. 1b). It is clear that no gas flow is present in the solid interconnect. The continuity, momentum and species equations are then blocked out and only the heat conduction equation, derived from the energy equation, is solved for this domain. As mentioned earlier, the physical/transport properties of the fuel gas mixture are variable. These parameters depend on the position in the duct, and the fuel species mass fraction and temperature as well. All the parameters are calculated and updated during iterations of the calculation.

In this investigation, a uniform grid point distribution in the cross section is applied. To obtain finer meshes in the entrance region of the duct, a non-uniform distribution of grid points with an expansion factor is implemented for the main flow direction. In order to evaluate the performance of the numerical method and code, test calculations considering grid sensitivity, code performance and validation were carried out. It is clear that the predictions do not change significantly in terms of fuel species distributions, when the number of grid points is increased beyond

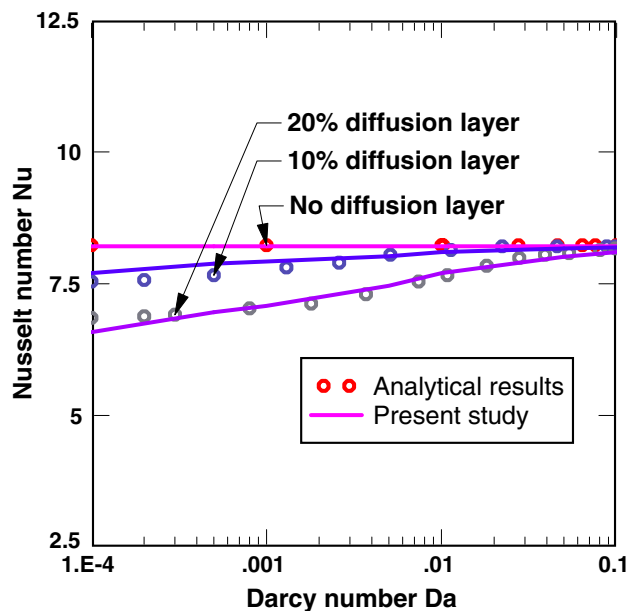


**Fig. 2** Fully developed Nusselt number  $Nu$  variation in a parallel plate duct with Darcy number ( $Da = \beta/h^2$ ), compared with analytical results from [14]

$70 \times 70 \times 50$  ( $70 \times 50$  for the cross section, 70 for the main flow direction). Calculations have been carried out for fully developed conditions in a parallel plate duct for various thicknesses of the porous layer and the same boundary conditions of constant heat flux on the walls. The comparison shows that the computed values of Nusselt numbers  $Nu$  agree well with the analytical ones, as shown in Fig. 2.

It is worth to note that the current code has been applied to model the two phase flow involving water phase change in the porous cathode and effects on the overall performance of proton exchange membrane fuel cells (PEMFCs). Comparisons with other models show qualitative agreement regarding the 10% liquid water saturation in the porous layer close to the exit. Furthermore, the polarization curves are compared with experimental data. It is revealed that the agreement between calculations and experimental results is good [15].

Parameters of ITSOFCs and the porous anode configuration from common literature are applied as a base case in this study. Duct geometries are: length of the duct  $L = 20$  mm; width of the porous layer  $a = 2$  mm, and its thickness  $h_p = 2$  mm; while the width of the flow duct is  $b = 1$  mm, and its height  $h_d = 1$  mm. Fuel gas inlet conditions are: temperature  $T_{in} = 800^\circ\text{C}$ , partially (30%) prereformed methane/steam mixture with:  $Re_{in} = 50$ , molar concentration  $X_{H_2}:X_{CH_4}:X_{CO}:X_{H_2O}:X_{CO_2} = 0.280:0.171:0.023:0.473:0.053$ ; in the porous layer, typical values are employed for porosity  $\varepsilon = 0.5$ , tortuosity  $\tau = 3$ , and permeability  $\beta = 2 \times 10^{-10} \text{ m}^2$ ; The binary

**Table 2** Binary diffusivity of the  $i$ th fuel gas species at  $T = 1123.15 \text{ K}$ ,  $p = 1.013 \text{ bar}$  [4]

$i/j$	$D_{i,j} \text{ (m}^2/\text{s)}$	$i/j$	$D_{i,j} \text{ (m}^2/\text{s)}$
CH <sub>4</sub> /CO	3.47e-05	CO/H <sub>2</sub>	11.92e-05
CH <sub>4</sub> /H <sub>2</sub> O	4.30e-05	CO/CO <sub>2</sub>	2.59e-05
CH <sub>4</sub> /H <sub>2</sub>	11.04e-05	H <sub>2</sub> O/H <sub>2</sub>	14.10e-05
CH <sub>4</sub> /CO <sub>2</sub>	2.88e-05	H <sub>2</sub> O/CO <sub>2</sub>	3.38e-05
CO/H <sub>2</sub> O	4.15e-05	H <sub>2</sub> /CO <sub>2</sub>	10.23e-05

diffusion coefficients of the fuel species are shown in Table 2. In this study, a constant current density  $i = 0.6 \text{ A/cm}^2$  is prescribed.

Three characteristic ratios, having significant effects on various transport processes and chemical reactions as discussed later in this paper, are defined in this section. These are the hydraulic diameter ratio  $D_{hr}$  (ratio of the porous anode diameter to the flow duct diameter), the permeation length ratio  $PL_r$  (ratio of the fuel flow duct width to the porous anode layer width), and the permeation rate ratio  $PR_r$  (ratio of the entrance pressure gradient to permeation resistance).

$$D_{hr} = D_{hp}/D_{hd} \quad (25)$$

$$PL_r = a/b \quad (26)$$

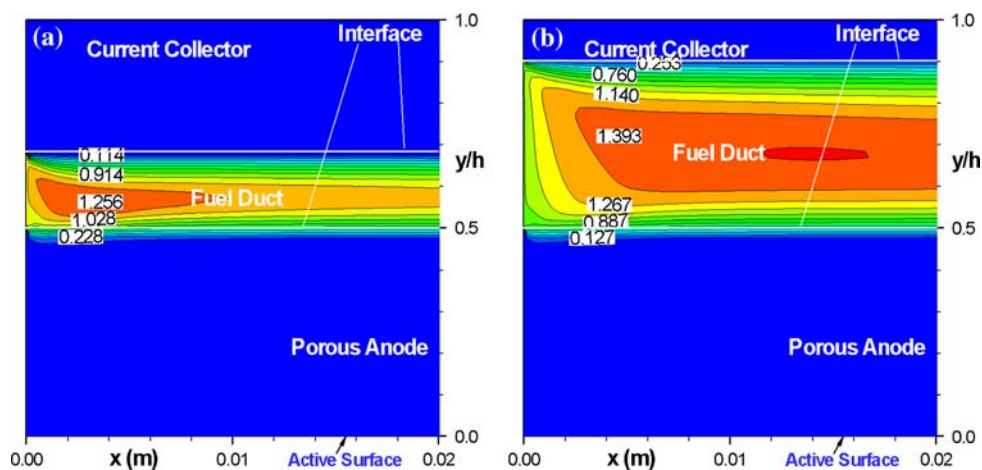
$$PR_r = (\rho U_{in}^2/2h_p)/(\mu U_{in}/\beta_i) = (\rho\beta_i U_{in})/(2\mu h_p) \quad (27)$$

$D_{hp}$  in Eq. 25 is the hydraulic diameter of the porous anode layer,  $D_{hd}$  the hydraulic diameter of the fuel flow duct;  $a$  in Eq. 26 is the width of gas flow duct,  $b$  the width of the porous anode;  $h_p$  in Eq. 27 is the thickness of the porous layer. It is clear that both diameter ratio  $D_{hr}$  and permeation length ratio  $PL_r$  are related to the fuel flow duct and porous anode configurations, to account for the characteristics of the permeation area and length, respectively. The permeation rate ratio  $PR_r$  considers the characteristics of the porous anode material (such as the permeability  $\beta_i$ ) and duct operation parameter (such as the inlet velocity  $U_{in}$ ). Based on the base case data above, the three characteristics ratios are:  $D_{hr} = 2$ ,  $PL_r = 2$  and  $PR_r = 0.012$ , respectively. It should be noted that parameter studies are conducted for various ratios by changing  $h_d$ ,  $b$ ,  $h_p$ ,  $\beta$  and  $U_{in}$ , respectively.

### 3.1 Effects of the diameter ratio ( $D_{hr} = 2.33$ , 1.24 vs. 2.0)

To investigate effects of the diameter ratio on the transport phenomena and chemical reactions, the height of fuel flow duct  $h_d$  is varied. Figure 3 shows velocity contours for the cases of  $D_{hr} = 2.33$  ( $h_d = 0.75 \text{ mm}$ ) and  $D_{hr} = 1.24$  ( $h_d = 1.6 \text{ mm}$ ). It should be noted that the height of the

**Fig. 3** Velocity contours for the cases of: **a**  $D_{hr} = 2.33$  ( $h_d = 0.75$  mm); **b**  $D_{hr} = 1.124$  ( $h_d = 1.6$  mm)



upper solid plate was changed accordingly to keep the total height of the current collector and the fuel flow duct constant.

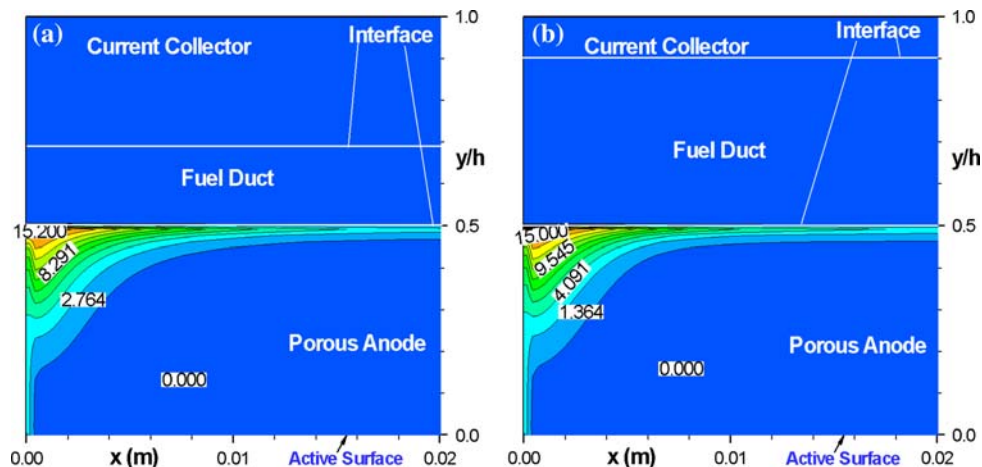
As revealed in [7] for the base condition, gas flow and heat transfer in the composite ducts are affected by the internal reforming reactions in the porous anode layer and the electrochemical reactions close to the active surface. Due to the permeation and mass generation/consumption effects, the uniform distribution and the symmetry of the axial velocity associated with a pure forced duct flow does no longer exist, and the position of the maximum contour values shifts away from the central plane. More mass is permeated into the porous anode layer at the entrance area because the largest pressure gradient between the flow duct and the porous layer occur here [6]. As a consequence, part of the boundary is shifted into the porous anode layer, which can be verified by a change of the boundary layer thickness close to the interface. Because the pressure in the fuel flow duct will fall due to friction, a decreased pressure gradient along the main stream is expected. Consequently, gas permeation decreases and becomes weaker. The axial

velocity magnitude of the fuel mixture decreases rapidly in the porous layer as well.

As shown in Fig. 3, the velocity contours for big or small  $D_{hr}$  have a similar trend as that of the base case [7], i.e., there is no symmetry of the axial velocity and the position of the maximum values shifts away from the physically central plane. This effect is more significant for the big  $D_{hr}$  case (Fig. 3a), if compared to the one with small  $D_{hr}$  (Fig. 3b). More critically, more fuel is permeated to and kept in the porous anode region, as shown in Fig. 3a with smaller velocity contours than those in Fig. 3b. This may be due to the fact that the fuel flow duct in Fig. 3a is small if compared to the porous anode layer.

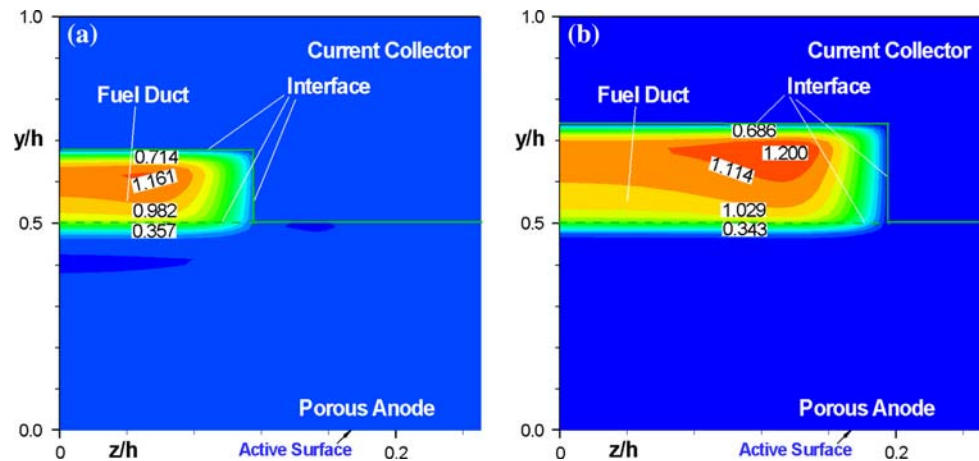
It is found, from Fig. 4, that almost the same steam reforming reaction rates are obtained when the hydraulic diameter ratio  $D_{hr}$  changes. This finding is also true for the water gas-shift reaction, in terms of maximum reaction rates, see Table 3. This means that the diameter ratio has more significant effects on the fuel gas flow in both fuel flow duct and the porous anode layer than those on the overall chemical reactions. It is believed that the high

**Fig. 4** Steam reforming reaction rate  $R_r$  at: **a**  $D_{hr} = 2.33$  ( $h_d = 0.75$  mm); **b**  $D_{hr} = 1.24$  ( $h_d = 1.6$  mm)



**Table 3** Effects of the diameter ratio  $D_{hr}$  on the predicted reaction performance

	Steam reforming reaction rate, $R_{r,max}$ , mol/(m <sup>3</sup> s)	Water gas-shift reaction rate, $R_{s,max}$ , mol/(m <sup>3</sup> s)	Methane conversion, %
$D_{hr} = 1.24$	15.193	34.193	35.075
$D_{hr} = 2$ (Base case)	15.217	35.144	42.566
$D_{hr} = 2.33$	15.209	35.040	50.652

**Fig. 5** Distribution of velocity contours at the inlet cross section for the cases of: **a**  $PL_r = 2.67$  ( $b = 0.75$ ); **b**  $PL_r = 1.25$  ( $b = 1.6$ )

methane conversion obtained in the case of big  $D_{hr}$  is mainly due to the fact that the fuel flow rate is small when the fuel flow duct is small or the diameter ratio  $D_{hr}$  is big.

It should be noted that the methane conversion efficiency is defined in the conventional manner, i.e., the ratio of mole  $CH_4$  fraction difference between the anode inlet and exit, and the fraction at the inlet,  $(X_{CH_4, inlet} - X_{CH_4, exit})/X_{CH_4, inlet}$ .

### 3.2 Effects of permeation length ratio ( $PL_r = 2.67$ , 1.25 vs. 2.0)

Effects of the permeation length ratio have been investigated as well by varying the width of the fuel flow duct  $a$ , while other ratios are kept constant. Permeation length ratios  $PL_r = 2.67$  ( $b = 0.75$ ) and  $PL_r = 1.25$  ( $b = 1.6$ ) are employed, and the predicted performance is compared with that of the base case ( $PL_r = 2.0$ ,  $b = 1$  mm). From Fig. 5, it is found that the cross-section velocity profiles are similar to each other for different permeation length ratios. Moreover, the steam reforming reaction rates for the case with big permeation length ratio (Fig. 6a) is almost in the same order as that achieved in the case with small permeation length ratio (Fig. 6b). This conclusion is true for the water gas-shift reaction, in terms of maximum reaction rates, see Table 4. On the other hand, the overall chemical reaction performance with big permeation length ratio achieved higher methane conversion than those with small permeation length ratios. This means that permeation

length ratio has more significant effects on the overall chemical reactions.

### 3.3 Effects of the permeation rate ratio

The effects of the permeation rate ratio on the fuel gas flow are shown and discussed in the following section. It is noted from Fig. 7a that, by increasing the permeability, fuel gas permeation to the porous layer is big, i.e., the length having a axial velocity in the porous anode close to the fuel flow duct is longer, if compared to the case with a small permeability shown in Fig. 7b. This is so because the permeability is a term used for the conductivity of the porous medium with respect to permeation by a fluid. It is known that a big permeability of a porous layer allows more gas to pass at the same pressure gradient. Consequently, more fuel gas is permeated from the fuel flow duct, and the gas convection can be found with bigger velocities in the porous layer close to the fuel flow duct at the entrance region. Certain impacts on the change of the axial velocity distribution are expected for both the fuel flow duct and the porous anode layer, when the permeability is large.

As a consequence, more significant impacts on the internal reforming reactions and fuel gas distribution are expected for the case of the larger permeability. From Fig. 8a, it is found that the steam reforming reaction happens deeply in the porous anode, if compared with the case shown in Fig. 8b for small permeability. As for this case,



**Fig. 6** Distribution of steam reforming reaction at the inlet cross section for the cases of: **a**  $PL_r = 2.67$  ( $b = 0.75$ ); **b**  $PL_r = 1.25$  ( $b = 1.6$ )

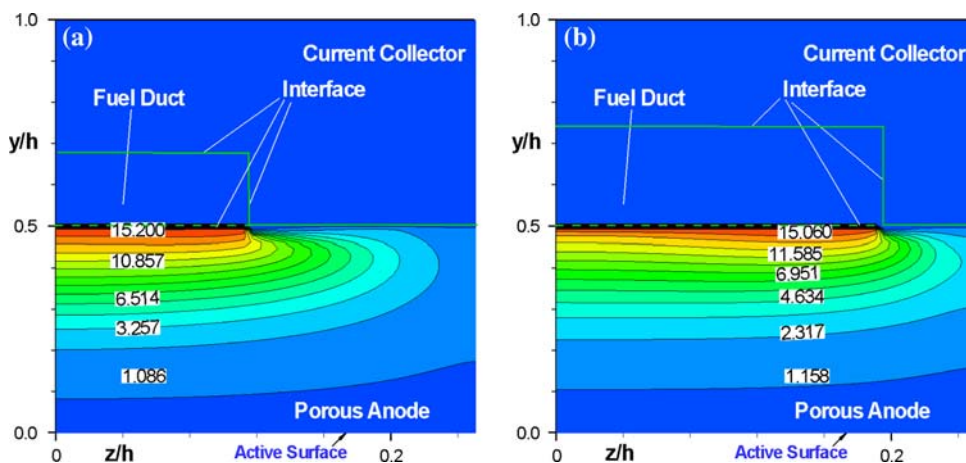
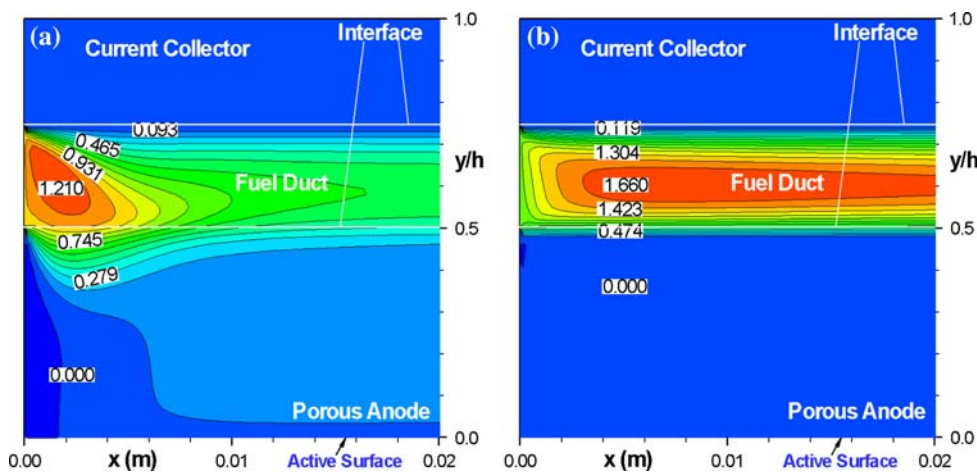


**Table 4** Effects of permeation length ( $PL_r = 2.67, 1.25$  vs. 2.0) on the reaction performance

	Steam reforming reaction rate, $R_{r,max}$ , mol/(m <sup>3</sup> s)	Water gas-shift reaction rate, $R_{s,max}$ , mol/(m <sup>3</sup> s)	Methane conversion, %
$PL_r = 2.67$	15.328	35.870	52.075
$PL_r = 2$ (Base case)	15.217	35.144	42.566
$PL_r = 1.25$	15.062	34.444	27.984

**Fig. 7** Effects of the permeation rate ratio (permeability) on the dimensionless axial velocity contours at: **a**  $\beta = 2.0 \times 10^{-9} \text{ m}^2$ ; **b**  $\beta = 5.0 \times 10^{-11} \text{ m}^2$



better utilization of catalytic surfaces in the porous anode can be expected, which can be verified by the CH<sub>4</sub> distribution in Fig. 9a. For the case with a small permeability as shown in Fig. 9b, a large amount of CH<sub>4</sub> is reacted in the interface region of the porous layer close to the fuel duct, which is reflected by a sharp decrease of CH<sub>4</sub> mass concentration. This region is confined only up to around 200–300 μm into the anode porous layer at most of the stations along the main flow stream, except at the inlet areas where the reactions take place more deeply into the porous anode. There is hardly any methane reaching the active surface after the first 10% of the duct length.

The variation in temperature distribution can also be observed in the vertical direction with a slightly larger

value close to the active surface. These are created by the heat generation due to the electrochemical reactions close to the active surface. Figure 10 shows the temperature distribution to reveal the permeability effects. It is found that the duct employing small permeability have high temperatures in both the fuel flow duct and the porous anode. For instance, the maximum temperature appearing in the active surface corner at the exit is 813°C in Fig. 10b, compared to 804.6°C for the case with big permeability (see Fig. 10a). It is so because the steam reforming reaction is more deeply penetrated into the porous anode, where the more heat is consumed.

Effects of inlet velocity on the reforming performance are shown in Figs. 11 and 12. Permeation rate ratios

**Fig. 8** Effects of the permeation rate ratio (permeability) on the steam reforming reaction rate  $R_r$  distribution at:

- a**  $\beta = 2.0 \times 10^{-9} \text{ m}^2$ ;  
**b**  $\beta = 5.0 \times 10^{-11} \text{ m}^2$

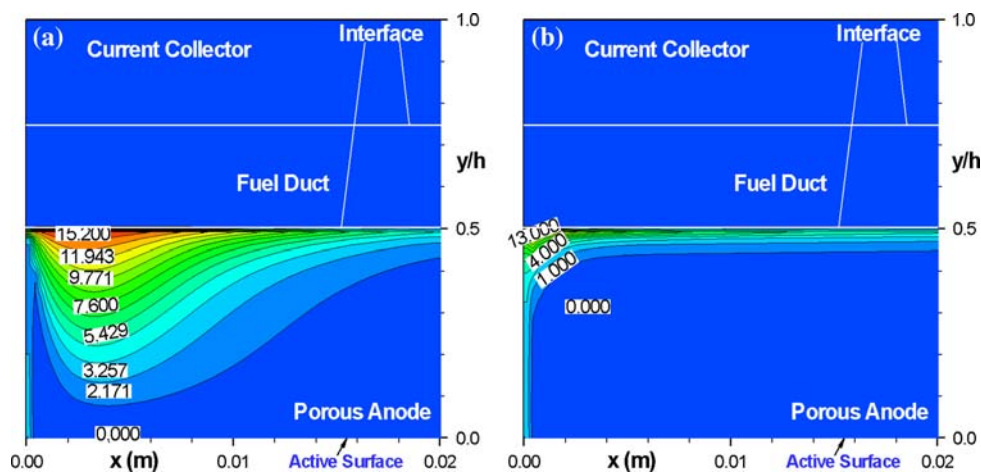


**Fig. 9** Effects of the permeation rate ratio (permeability) on  $\text{CH}_4$  mass distribution at:

- a**  $\beta = 2.0 \times 10^{-9} \text{ m}^2$ ;  
**b**  $\beta = 5.0 \times 10^{-11} \text{ m}^2$

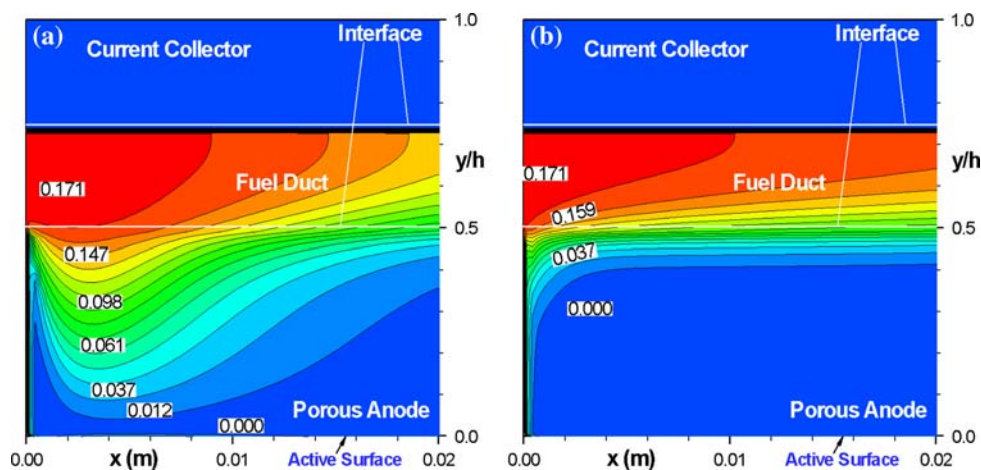
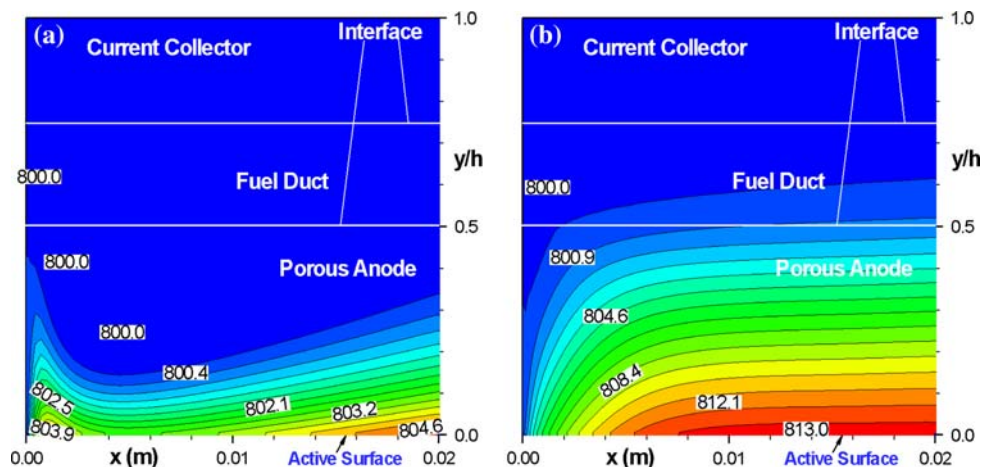


**Fig. 10** Effects of the permeation rate ratio (permeability) on temperature distribution at: **a**  $\beta = 2.0 \times 10^{-9} \text{ m}^2$ ; **b**  $\beta = 5.0 \times 10^{-11} \text{ m}^2$



$PR_r = 0.006$  ( $U_{in} = 25 \text{ m/s}$ ) and  $PR_r = 0.024$  ( $U_{in} = 100 \text{ m/s}$ ) have been employed to compare with each other, i.e.,  $PR_r = 0.012$  and  $U_{in} = 50 \text{ m/s}$ . It is revealed that, in the entrance region, small  $PR_r$  has a small steam reforming reaction rate in Fig. 11a compared to the case in Fig. 11b with a big inlet velocity case. It is because the fuel gas

permeation to the porous anode is small as revealed in [6]. Big inlet velocity on the other hand has more significant effects not only on the fuel gases permeation to the porous anode for the reactions, but also on the convection (the fuel flow rate) in the gas flow duct. It is then noted from Fig. 12a that the exit  $\text{CH}_4$  mole fraction (big methane conversion) is

**Fig. 11** Effects of the permeation rate ratio (inlet velocity) on the steam reforming reaction distribution at inlet velocity of: **a**  $U_{in} = 25$  m/s; **b**  $U_{in} = 100$  m/s

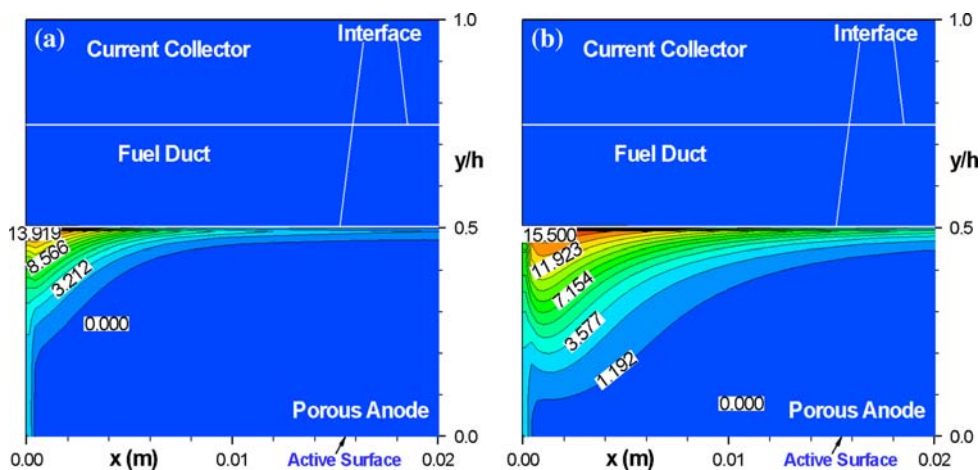
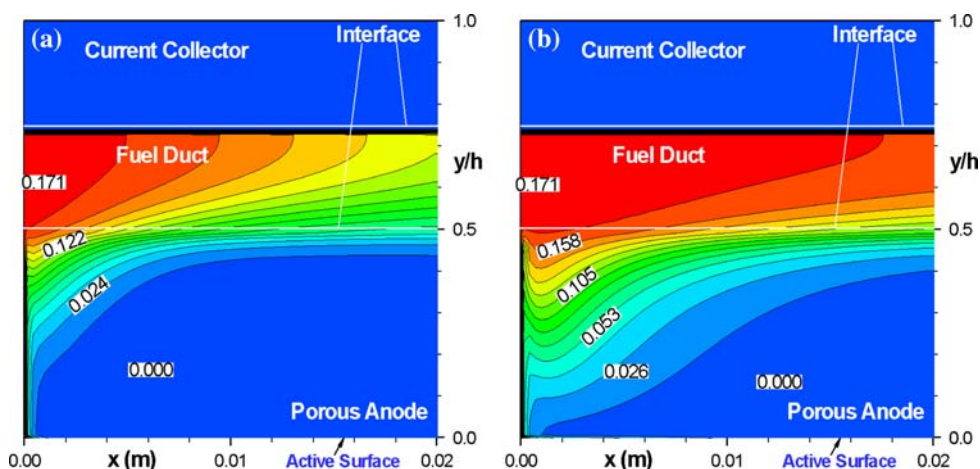


**Fig. 12** Effects of the permeation rate ratio (inlet velocity) on the  $\text{CH}_4$  distribution at inlet velocity of: **a**  $U_{in} = 25$  m/s; **b**  $U_{in} = 100$  m/s



small even the reforming reaction rate is small compared to the case in Fig. 12b. It means that the  $\text{CH}_4$  mass fraction distribution (methane conversion) is controlled by the combined effects of the reforming reactions in the porous anode and convective flow (the fuel flow rate) along the flow direction downstream the fuel gas flow duct.

Figure 13 shows the temperature distribution to reveal the inlet velocity effects. As found in Figs. 11b and 12b for big inlet velocities, the steam reforming reaction is more deeply penetrated into the porous anode, and the more heat is consumed. Consequently the cool region with low temperature becomes larger in Fig. 13b, compared to that in Fig. 14a with small inlet velocity. It is also clear that the maximum temperature is lower for the case of big inlet velocity in Fig. 13b.

To investigate effects of the porous anode thickness on the transport processes and the coupled chemical reactions, the height of porous anode  $h_p$  was varied while other parameter ratios were kept constant. It is noted that the ducts employing thin porous layers (thickness  $h_p = 0.86$  and  $0.5$  mm, respectively, vs.  $2.0$  mm) predict very similar

velocity contour profiles, as shown in Fig. 14. However for the case of the thinner porous anode (Fig. 14b), fuel gas velocity is big in the porous anode layer close to the fuel flow duct.

It is clear that the distribution of steam reforming reaction rates in Fig. 15 holds a similar trend, i.e., strong steam reforming reaction appears in the interface region of the porous anode close to the fuel flow duct for both configurations in Figs. 15a and b. On the other hand, non-reaction zone (with zero reaction rates) is small for the case with a thin porous anode in Fig. 15b, compared to the case with a big  $h_p$  value shown in Fig. 15a. However, the supplied methane is completely reformed in the case of the thick porous anode (Fig. 16a), while there is around 2% of unreformed methane left and reached the active electrochemical reaction surface (the bottom surface), i.e., the unreformed methane can be found in the region close to the active surface, see Fig. 16b. It may be due to the fact that the reaction region in the porous anode is small in this case, in terms of the porous anode thickness. By comparing to Fig. 16b, it is worth to note that the steam reforming

**Fig. 13** Effects of the permeation rate ratio (inlet velocity) on temperature distribution at: **a**  $U_{in} = 25$  m/s; **b**  $U_{in} = 100$  m/s

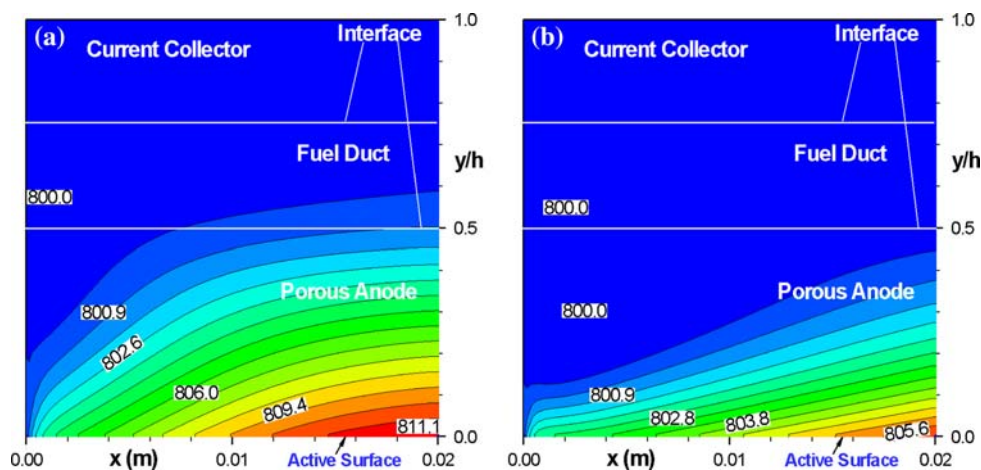


**Fig. 14** Effects of the permeation rate ratio (porous anode thickness) on the velocity contours for the cases of: **a**  $h_p = 0.86$  mm; **b**  $h_p = 0.5$  mm

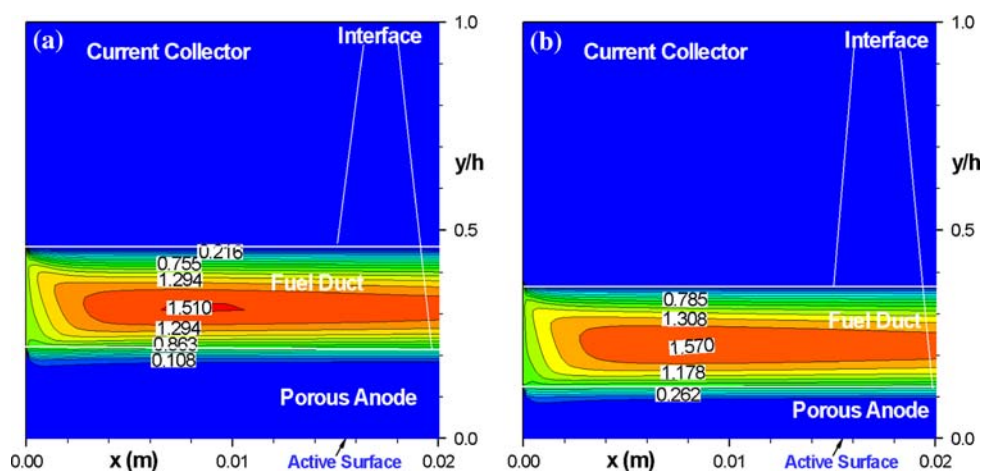
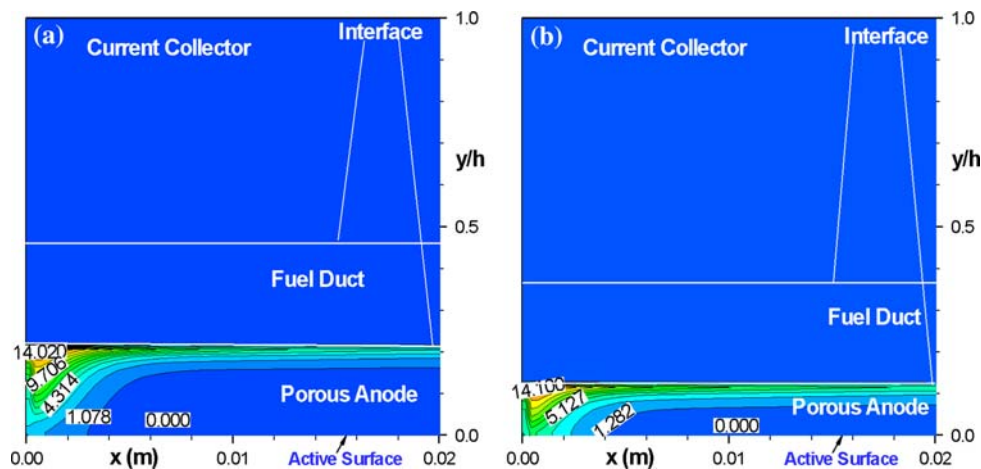


**Fig. 15** Effects of the permeation rate ratio (porous anode thickness) on the steam reforming reaction distribution at: **a**  $h_p = 0.86$  mm; **b**  $h_p = 0.5$  mm



reaction rate depends on not only the methane mass fraction distribution, but also other parameters, such as local temperature and species partial pressure etc.

The overall reforming reaction performance achieved in both cases is similar to the one by the base case, in terms of the methane conversion efficiency (41.101, 39.572 vs.

42.566% in Table 5), and the maximum reaction rates of the steam reforming and the water gas-shift reactions.

Figure 17 shows the temperature distribution to reveal the porous anode thickness effects. It is found that the anode ducts employing thin porous layers have similar temperatures in both the fuel flow duct and the porous

**Fig. 16** Effects of the permeation rate ratio (porous anode thickness) on  $\text{CH}_4$  mass fraction distribution at: **a**  $h_p = 0.86$  mm; **b**  $h_p = 0.5$  mm

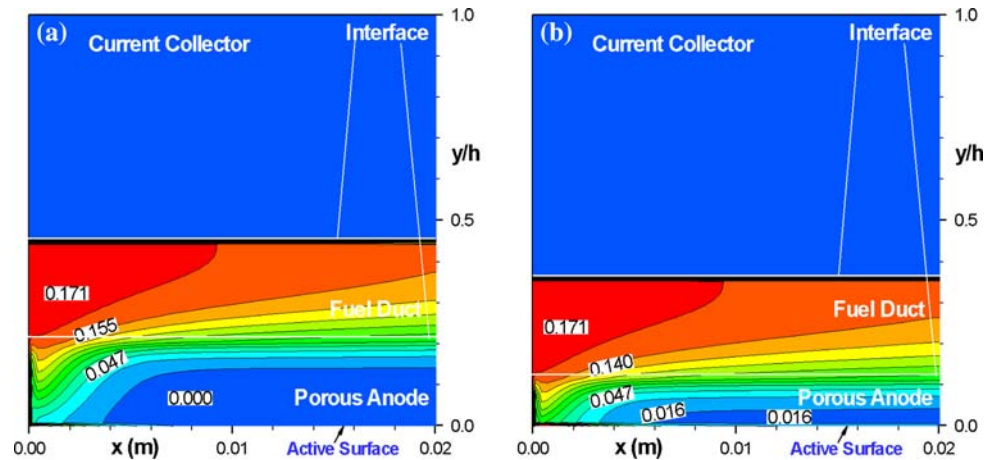
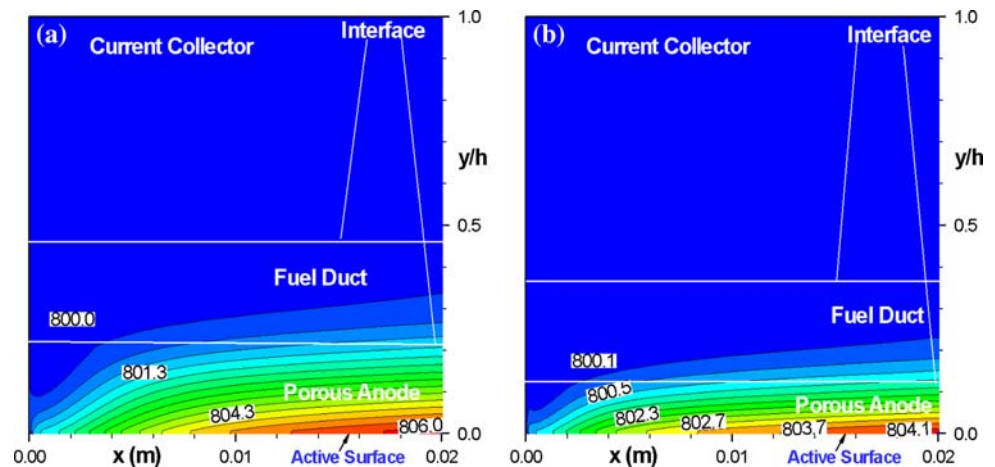


**Table 5** Effects of the thickness of the porous anode on the predicted reaction performance

	Steam reforming reaction rate, $R_{r,\max}$ , mol/(m <sup>3</sup> s)	Water gas-shift reaction rate, $R_{s,\max}$ , mol/(m <sup>3</sup> s)	Methane Conversion, %
Base case, $h_p = 2$ mm	15.217	35.144	42.566
$h_p = 0.86$ mm	15.098	34.687	41.101
$h_p = 0.5$ mm	14.959	34.230	39.572

**Fig. 17** Effects of the permeation rate ratio (porous anode thickness) on temperature distribution at: **a**  $h_p = 0.86$  mm; **b**  $h_p = 0.5$  mm



catalyst layers. For instance, the maximum temperatures appearing in the active plate corner (the bottom plate) at the exit are 806 and 804°C for thin porous layers, compared to 809°C for the base condition (not shown). It is so because the overall chemical reaction performance for the above cases holds a very similar figure, as shown in Table 5, and consequently similar heat consumption and heat transfer are expected for these cases.

As discussed above, it is clear that the thickness of the porous anode has different roles in the overall chemical reaction performance and the transport processes. It is due to the fact that the thickness of the porous anode is involved in both the diameter ratio and permeation rate

ratio, i.e., a thin porous layer generates a smaller diameter ratio  $D_{hr}$ , however a bigger permeation rate ratio. Further study is suggested to find an optimal thickness of the porous anode, in conjunction with the catalyst loading and distribution.

#### 4 Conclusions

A three-dimensional CFD method has been developed to analyze the parameter effects on chemical-reaction-coupled gas flow and heat transfer processes in a composite anode duct in intermediate temperature planar design

SOFCs. Momentum and heat transport together with gas species equations are solved by coupled source terms, variable thermo-physical and transport properties of the fuel gas species. The model offers the possibilities to reveal significant effects of effects of the characteristic parameters involving SOFC design and operating aspects by taking into account the internal reforming reactions and the electrochemical reactions.

The predicted results show that, at most regions apart from the cell inlet, the internal reforming reactions are confined in a thin porous anode layer close to the fuel flow duct. Transport processes of the fuel gas species and temperature distribution are affected by both the internal reforming reactions and the electrochemical reaction. By varying one or more of the characteristic ratios identified in this paper, effects of design and operating parameters on the transport processes coupled by various reactions have been investigated in terms of velocity and temperature distributions and fuel gas species mass fraction, and overall reaction performance. Optimal characteristic ratios involving SOFC configuration design and operating parameters may be achieved by considering the catalyst loading and distribution in the porous anode.

**Acknowledgments** One of the authors (J. Yuan) gratefully acknowledges the support of K. C. Wong education foundation, Hong Kong. The Swedish Research Council (VR) supports the current research.

## References

1. Wang WG, Mogensen M (2005) High-performance Lanthanum-ferrite-based cathode for SOFCs. *Solid State Ion* 176:457–462
2. Hussain MM, Li X, Dincer I (2006) Mathematical modeling of planar solid oxide fuel cells. *J Power Sources* 161:1012–1022
3. Virkar AV, Chen J, Tanner CW, Kim JW (2000) The role of electrode microstructure on activation and concentration polarizations in solid oxide fuel cells. *Solid State Ion* 131:189–198
4. Yakabe H, Hishinuma M, Uratani M, Matsuzaki Y, Yasuda I (2000) Evaluation and modeling of performance of anode-supported solid oxide fuel cell. *J Power Sources* 86:423–431
5. Lehnert W, Meusinger J, Thom F (2000) Modelling of gas transport phenomena in SOFC anodes. *J Power Sources* 87:57–63
6. Ackmann T, Haart LGJ, Lehnert W, Thom F. Modelling of mass and heat transport in thick-substrate thin-electrolyte layer SOFCs. In: *Proceedings of the 4th European solid oxide fuel cell forum 2000*, Lucerne/Switzerland, pp 431–438
7. Yuan J, Rokni M, Sundén B (2003) Three-dimensional computational analysis of gas and heat transport phenomena in ducts relevant for anode-supported solid oxide fuel cells. *Int J Heat Mass Transf* 46:809–821
8. Yakabe H, Ogiwara T, Hishinuma M, Yasuda I (2001) 3-D model calculation for planar SOFC. *J Power Sources* 102:144–154
9. Barzi YM, Ghassemi M, Hamed MH, Afshari E (2007) Numerical analysis of output characteristics of a tubular SOFC with different fuel compositions and mass flow rates. In: Eguchi K, Singhal SC, Yokokawa H, Mizusaki J (eds) *Proceedings of solid oxide fuel cells 10 (SOFC-X)*. ECS Transactions 7(1):1919–1928
10. Yuan J, Faghri M, Sundén B (2005) On heat and mass transfer phenomena in PEMFC and SOFC and modeling approaches. In: Sundén B, Faghri M (eds) *Transport phenomena in fuel cells*. WIT Press
11. Aguiar A, Adjiman CS, Brandon NP (2004) Anode-supported intermediate temperature direct internal reforming solid fuel cell. I: model-based steady-state performance. *J Power Sources* 138:120–136
12. Mostinsky IL (1996) Diffusion coefficient. In: Hewitt GF, Shires GL, Polezhaev YV (eds) *International encyclopedia of heat & mass transfer*. CRC Press, Florida
13. Ferguson JR, Fiard JM, Herbin R (1996) Three-dimensional numerical simulation for various geometries of solid oxide fuel cells. *J Power Sources* 58:109–122
14. Alazmi B, Vafai K (2001) Analysis of fluid flow and heat transfer interfacial conditions between a porous medium and a fluid layer. *Int J Heat Mass Transf* 44:1735–1749
15. Yuan J, Sundén B, Hou M, Zhang H (2004) Three-dimensional analysis of two-phase flow and its effects on the cell performance of PEMFCs. *Num Heat Transf (Part A)* 46:669–694